Photocatalytic Efficiency Variability in TiO2 Particles

2 AUTHORS, INCLUDING:

James R Bolton
University of Alberta

315 PUBLICATIONS **10,087** CITATIONS

Photocatalytic Efficiency Variability in TiO$_2$ Particles
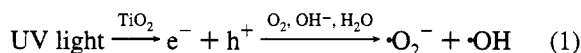
Georg Riegel and James R. Bolton*

Photochemistry Unit, Department of Chemistry, The University of Western Ontario, London, Ontario, Canada N6A 5B7

Received: September 13, 1994; In Final Form: December 8, 1994[®]

The pre-steady-state photoproduction of hydroxyl radicals (•OH) from various TiO$_2$ samples in an aqueous suspension was investigated, using spin trapping with electron paramagnetic resonance (EPR) spectroscopy for detection. This pre-steady-state •OH production does not require the presence of a dissolved electron acceptor and thus depends only on processes of oxidation and recombination. The efficiency variations that characterize the steady state, in particular for samples in the anatase and rutile crystal forms of TiO$_2$, are also found under pre-steady-state conditions. Therefore, we propose that variations in the rate constants related to recombination and/or oxidation cause the observed variability in steady-state photocatalytic efficiency. An analysis of the pre-steady-state and steady-state results, based on a simple kinetic model, indicates that the observed variability arises specifically from variations in the rate constant for recombination. In addition, the role of the oxidative power of holes at the valence-band edge was gauged, using size-quantized rutile particles in the form of quantum wires, which were obtained from TiCl$_4$ hydrolysis. It is expected that almost the entire bandgap increase of ~0.14 eV is imparted to the hole oxidative power. Nonetheless, the effect on the photocatalytic efficiency does not appear to be significant.

1. Introduction

TiO$_2$ Photocatalysis. When exposed to suprabandgap radiation, titanium dioxide particles in an air-saturated aqueous environment induce the formation of hydroxyl (•OH) and superoxide (•O$_2^-$) radicals:[1,2]

$$\text{UV light} \xrightarrow{\text{TiO}_2} e^- + h^+ \xrightarrow{\text{O}_2, \text{OH}^-, \text{H}_2\text{O}} \cdot\text{O}_2^- + \cdot\text{OH} \quad (1)$$

where e$^-$ and h$^+$ denote the photogenerated conduction-band electrons and valence-band holes. The hydroxyl radical, which may result from several reaction paths, is thought to be the key species in the photocatalytic oxidation of organics on TiO$_2$.[1,3,4] These oxidation reactions may lead to the complete degradation ("mineralization") of the organic substrates[5] and have thus attracted much interest in the field of water decontamination.[3,6,7]

The quantum efficiency of these processes, that is, the rate at which the desired oxidation products are formed divided by the absorbed photon flux, varies over a wide range from one TiO$_2$ sample to another. In particular, particles in the anatase crystal form of TiO$_2$ are usually much more efficient than are particles in the rutile crystal form.[1,8-10] For a given TiO$_2$ sample, this efficiency is determined by the competition for carriers between the reactions of oxidation and reduction on the one hand and processes of recombination on the other hand. We shall include in the first category only those processes that lead to products that are stable during the observation time. All other carrier-induced processes are considered to be forms of recombination.

The aim of the present paper is to determine which of the three process categories is responsible for the observed efficiency variations in TiO$_2$ photocatalysis. In particular, it was of interest to investigate if the larger bandgap of anatase (3.23 vs 3.02 eV in rutile) is responsible for the greater efficiency of that crystal form. This had been suggested because of the larger reduction potential of electrons at the conduction-band edge of anatase.[9,11]

EPR/Spin Trapping. An excellent technique for studying the efficiency of •OH production is that of spin trapping with electron paramagnetic resonance (EPR) for detection.[12] This technique was developed by Janzen and Blackburn[13] and was first applied to TiO$_2$ photocatalysis by Jaeger and Bard.[1] In this case, the hydroxyl radicals, which are short-lived and difficult to detect directly, add to a "spin trap". A suitable spin trap leads to the formation of a stable free radical, called the "spin adduct", whose EPR spectrum is characteristic of the trapped •OH. In kinetic studies of •OH radical formation, one monitors the intensity of a given line in that spectrum over time.

Harbour *et al.*[14] found that 5,5-dimethyl-1-pyrroline *N*-oxide (DMPO) is a particularly effective spin trap for hydroxyl radicals. The addition of •OH to DMPO yields the spin adduct DMPO-OH according to the reaction
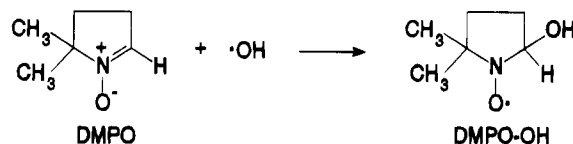
The reported rate constant for this reaction in homogeneous solution is 4.3 × 10^9 M^{-1} s^{-1}.[15] DMPO-OH exhibits the characteristic four-line 1:2:2:1 EPR spectrum shown in Figure 1. The heights of these lines are directly proportional to the DMPO-OH concentration. Other reactions between DMPO and •OH are also possible, and the actual fraction of DMPO-OH molecules among the reaction products is ~0.33.[16,17] This ratio is called the "trapping efficiency".

In addition, DMPO-OH may form through other pathways such as hole transfer to the NO group of DMPO, followed by hydrolysis. We shall assume that the sample-to-sample variations in the reaction paths and product ratios are small and that differences in the DMPO-OH formation rates thus reflect characteristic differences in the efficiencies of hole transfer.

Simplified Steady-State Kinetics. Gerischer[18] proposed a simple kinetic scheme that describes the essential features of

4216 *J. Phys. Chem., Vol. 99, No. 12, 1995*

Riegel and Bolton
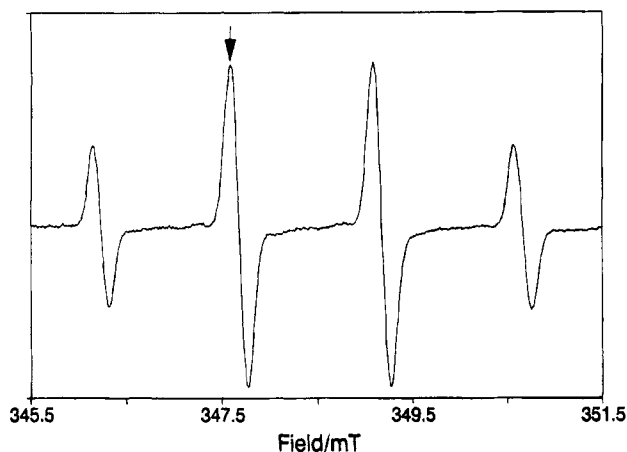
Figure 1. Four-line EPR spectrum of DMPO-OH, wherein the hyperfine splitting constants are $a^N = a^H = 1.49$ mT. The arrow indicates the line whose height was monitored in the kinetic experiments of this study.

steady-state TiO$_2$ photocatalysis. Adapted to our case, where the stable product of interest is DMPO-OH, this scheme is

$$TiO_2 + h\nu \rightarrow h^+ + e^- \qquad I_a \qquad (2)$$

$$h^+ + OH^- \text{ (or } H_2O) \rightarrow \cdot OH \qquad k_t[h^+] \qquad (3)$$

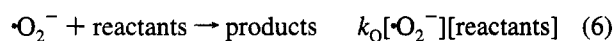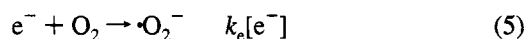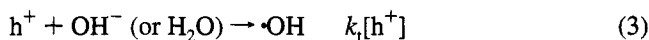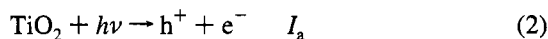$$\cdot OH + DMPO \rightarrow DMPO\text{-}OH \qquad k_h[\cdot OH] \qquad (4)$$

$$e^- + O_2 \rightarrow \cdot O_2^- \qquad k_e[e^-] \qquad (5)$$

$$\cdot O_2^- + \text{reactants} \rightarrow \text{products} \qquad k_O[\cdot O_2^-][\text{reactants}] \qquad (6)$$

$$e^- + \cdot OH \rightarrow OH^- \qquad k_r[e^-][\cdot OH] \qquad (7)$$
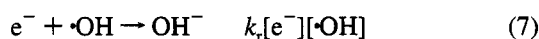
where the hole acceptors and products are assumed to be adsorbed at the particle surface. The rate expression for each reaction is given on the right-hand side of the respective equation.

This model explicitly assumes pseudo-first-order rate constants for the overall processes of formation and dissolution of the carrier transfer products. In particular, we include the sample-specific density of adsorbed OH$^-$ in the pseudo-first-order rate constant k_t. This approach is discussed in section 4.

Reaction 6 represents the reactions that involve $\cdot O_2^-$, including the corresponding recombination reactions with holes and hole products. Gerischer[18] assumed the surface concentration of $\cdot O_2^-$ to be negligible and that these reactions should therefore play no role. In this model, reaction 7 represents the dominant path of recombination. The relevance of recombination routes involving $\cdot O_2^-$ is investigated below.

The actual carrier kinetics are certainly more complex, and they may be determined by steps other than those depicted above. In particular, the question regarding the physical location of the critical reaction steps is one that has attracted much interest.[19-22] However, it should be noted that any model that assumes pseudo-first-order transfer kinetics and second-order recombination kinetics will result in the same kinetic features. With these conditions, which we shall discuss in section 4, we have at steady state

$$k_h[\cdot OH] = k_e[e^-] \qquad (8)$$

and

$$I_a = k_h\left(1 + \frac{k_r}{k_e}[\cdot OH]\right)[\cdot OH] \qquad (9)$$

By solving eq 9 for [$\cdot$OH], one obtains for the rate of DMPO-OH formation

$$k_h[\cdot OH] = [(1 + 4I_a/X)^{1/2} - 1]X/2 \qquad (10)$$

where

$$X = \frac{k_h k_e}{k_r} \qquad (11)$$

Thus, if the irradiance is sufficiently large, so that $4I_a/X \gg 1$, the rate is proportional to $I_a^{1/2}$, that is

$$k_h[\cdot OH] = (I_a X)^{1/2} \qquad (12)$$

whereas a linear relation between photocatalytic efficiency and irradiance should be obtained at low irradiance, where $4I_a/X \ll 1$.

Of particular interest is that this simple, but rather general, kinetic model predicts that the overall oxidation rate should depend only on I_a and on the quantity X (eq 11). Attempts to improve the steady-state photocatalytic efficiency of TiO$_2$ particles, either by catalyzing either of the two redox half-reactions or by decreasing the rate constant for recombination, should therefore be equally valid. This is of interest since to date much of the effort has focused on the reduction process, whose rate constant is far smaller than that for oxidation.[18,23-27] It is also clear that variations in the photocatalytic efficiency, found for differently prepared TiO$_2$ samples, could result from a variability in any one or several of the three rate constants in X. To our knowledge, no systematic investigation of this question has been undertaken to date.

2. Experimental Section

TiO$_2$ Samples. Table 1 describes the microcrystalline TiO$_2$ samples prepared in our laboratory; the characteristics of the investigated commercial samples are given in Table 2. The letter following the hyphen in each sample name indicates the dominant crystal phase, anatase (a) or rutile (r), in the respective sample. A capital letter indicates that the sample contains only the corresponding pure phase.

The characterization of sample P25-a, commonly known as "Degussa P25", is taken from a recent structural investigation which also showed that each primary particle in this sample contains only one crystalline phase.[28] Previously it had been suggested that this particularly efficient sample might be characterized by rutile overlayers on anatase particles.[29]

The synthesis of microcrystalline TiO$_2$ particles was based on common procedures for TiCl$_4$ hydrolysis.[30,31] Eleven milliliters (0.1 mol) of TiCl$_4$ (Fisher, Purified) was added dropwise to 1 L of deionized (Barnstead Thermolyne columns D8921 and D8922) and distilled water at a given temperature and under stirring. The samples were then aged in Nalgene bottles (1 L) at the same temperature. This temperature is given in Table 1 for four typical samples (I-R to IV-a), along with the aging times. After aging, the particles were washed 3 times by centrifugation and resuspension in water, increasing the suspension pH from 0.8 to 2.7. Powders were obtained by drying the sediment from the third centrifugation overnight in air at 72 °C. These powders were used in the experiments of

TABLE 1: Hydrolysis Parameters and Characteristics (TEM/XRD/BET/Diffuse Reflectance) of the Prepared Microcrystalline TiO₂ Samples[a]

sample	hydrolysis temp; aging time	crystal form; particle dimensions	bandgap U_g; crystallite size ratio R; specific surface area S
I-R	7 °C; 21 days	rutile needles (tightly aggregated); diameters 1.8 ± 0.5 nm	$U_g = 3.17 \pm 0.02$ eV; $S \approx 143$ m²/g
II-R	21 °C; 4 days	rutile needles (less aggregated); diameters 2.5 ± 0.8 nm	$U_g = 3.15 \pm 0.02$ eV; $S \approx 220$ m²/g
III-r	72 °C; 4 days	~85% rutile; mean diameter 5 nm	$R \approx 1.5$; $S \approx 126$ m²/g
IV-a	93 °C; 4 days	~70% anatase; mean diameter 5 nm	$R \approx 2$; $S \approx 158$ m²/g

[a] The last column gives the bandgap increase for samples of pure rutile or the ratio of the crystallite sizes for rutile and anatase, as applicable

TABLE 2: Characteristics of the Commercial Samples Studied

sample	source	crystal form (XRD)	mean particle diameter (TEM)	specific surface area (BET), m²/g
P25-a	Degussa	60–80% anatase, depending on the particular lot	15–20 nm; rutile crystallites ~70% larger than those of anatase	54.0
P9-R	P25 treated at 900 °C for 200 min	rutile only	(particle aggregates formed by sintering)	2.24
A-A	Aldrich	anatase only	100–200 nm	8.90
R-R	Aldrich	rutile only	>1 μm	2.64

sample characterization, as well as to prepare the suspensions used in the kinetic experiments.

Particle Sizes. Transmission electron microscopy (TEM) was performed using a Jeol JEM-100 CX II electron microscope. The images were recorded at a magnification of 2×10^5 and were further enlarged for analysis.

Crystal Forms and Crystallite Sizes. A Rigaku Rotaflex RU-200B, high-brilliance, rotating anode system, operated at 45 kV and 160 mA and characterized by an instrumental line width of 0.12° (2θ scale), was used in the X-ray diffraction (XRD) analysis. The K_{α_1} line of a Co source was employed, and the diffraction scans were taken at 10° min⁻¹ from 0° to 82° (2θ scale). Prior to analysis, the high-frequency noise was eliminated from these scans. The anatase/rutile ratios were obtained from the relative areas under the anatase (101) and rutile (110) diffraction lines, using a weighting factor of 1.26 for the rutile line.[32] The widths of these XRD lines provided the crystallite sizes for each phase, based on the Scherrer equation.[33]

Surface Areas. The specific surface areas of the samples were obtained from single-point Brunauer–Emmett–Teller (BET) isotherm measurements, using a Micromeritics TPD/TPR 2900 instrument with a 7:3 He:N₂ mixture at 77 K. Prior to the surface area measurement, each sample was outgassed at 350 °C for 30 min.

Semiconductor Bandgaps. Diffuse reflectance spectrometry was employed to determine the bandgaps of the samples in suspension, based on the blue shift in the interband transition onset. The quantitative method is described below. The spectra were obtained with a Shimadzu UV260 spectrophotometer equipped with an integrating sphere. For these measurements, the samples were suspended in 1 mM KH₂PO₄ buffer at a TiO₂ loading of ~1 g/L, attaining a neutral or slightly acidic pH. A quartz cuvette with an optical path length of 1 cm was used to hold the samples. No care had to be taken to prevent loss of UV light by transmission through the quartz cuvette since, as shown below, the effective penetration depth of UV light in TiO₂ suspensions with the employed loading is much smaller than the cuvette thickness.

Suspension Preparation. Aqueous suspensions of TiO₂ were prepared in 1 mM phosphate solutions, unless otherwise noted. Analytical reagent grade H₃PO₄, KH₂PO₄, and KOH were used for preparing these solutions at the desired pH values. For a typical measurement of the photocatalytic efficiencies at pH 7,

0.18 g of TiO₂ was added to 30 mL of the monobasic phosphate buffer (adjusted to pH 7). Intense ultrasound was applied to this suspension for 1 min by means of a sonicator rod (Artek "Sonic 300" at 70% maximum power). This procedure dispersed aggregated samples to a degree that allowed for reproducible EPR experiments.

Aliquots of the resulting suspension were diluted to the desired TiO₂ "loading" (typically 2 g/L) by adding buffer solution and a 1.5 mM stock solution of the spin trap (DMPO; Aldrich, 97%) which had been prepared in the same buffer. The final suspension volume for one set of EPR experiments (three runs per sample) was 15 mL, with a DMPO concentration of 0.5 mM.

Measurement of the ·OH Production. A Bruker ESP 300 EPR spectrometer, equipped with a TE 102 EPR cavity and operated at about 9.73 GHz, was employed to record the time evolution of DMPO-OH in the irradiated suspensions. For this purpose, the height of the EPR line indicated by the arrow in Figure 1 was monitored as a function of time. As shown below, the DMPO-OH concentration after ~1 s of irradiation is of particular interest. This concentration is denoted as "δOH", and its standard determination was performed as follows. The 1024 data points of 1 time scan were recorded with a signal collect time of 0.32 s and a time constant $\tau = 1.3$ s. The effect of τ is to average the EPR signal for the collect time at time t with the signal obtained at an earlier time $t - \Delta t$ by applying a weighting factor of exp(-$\Delta t/\tau$) to the latter. The resulting time scan was smoothed by applying a five-point, quadratic polynomial filter 5 times and then differentiated digitally. The peak value of this differentiated curve is the quantity δOH. This quantity may also be determined by measuring the DMPO-OH concentration after ~1 s or irradiation directly, using lower instrumental time settings. The equivalence of both methods is a result of the digital data acquisition and of the instrumental time settings. Examples for both methods are given below.

The samples were examined in a quartz EPR flat cell of 0.3-mm inner thickness and were replenished by means of a peristaltic pump and Teflon tubing, unless otherwise noted. The small thickness of the cell permitted the use of suspensions whose stability was limited under the experimental conditions: the measurements could be completed before changes in particle density became significant.

O₂ Concentration. Two methods were used for controlling the concentration of molecular oxygen in the suspensions. In
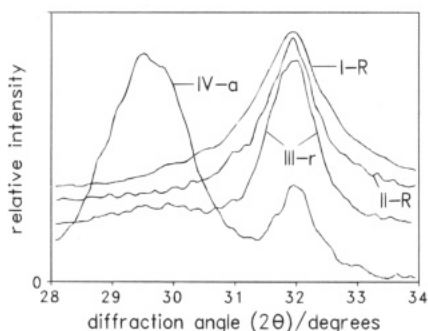
Figure 2. X-ray diffraction profiles of samples I-R through IV-a. The anatase (101) and rutile (110) lines occur at $2\theta = 29.6°$ and $32.0°$, respectively.

method 1, the suspensions were exposed to air or, alternatively, bubbled with air or with mixtures of prepurified O_2 and N_2 (O_2 contents of 0, 50, 75, 100%) for 40−60 min, prior to the EPR experiment. During the equilibration process, the suspensions were isolated from ambient air by glass wool stoppers. The gas mixtures were humidified by use of gas bubblers containing H_2O, before being passed through the suspensions, so as to prevent evaporation.

Method 2 was used to verify that no significant amount of molecular oxygen remained in the suspensions equilibrated with pure N_2. The method employed a modified experimental setup: the peristaltic pump was moved behind the EPR cell in the flow direction, and the samples were passed through glass tubing only, before reaching the EPR cell. This assembly was flushed with N_2-bubbled water, prior to the experiment. N_2 bubbling was undertaken for up to 20 h, taking the same precautions as in method 1.

Photon Flux. UV irradiation of the samples was carried out with a Ushio 200 W Xe/Hg lamp. The lamp output was collimated with a quartz lens, passed through a H_2O infrared filter of 10-cm path length, and then focused onto the EPR cell by means of a second quartz lens. Wire filters, placed in the collimated beam between the IR filter and the second lens, were used to control the irradiance. The approximate photon flux with $h\nu \geq 3.2$ eV that reached the suspension volume in the absence of wire filters was $\sim 2 \times 10^{-7}$ einstein s^{-1}, according to ferrioxalate actinometry.[34]

3. Results

Below, part A describes the microcrystalline samples obtained from $TiCl_4$ hydrolysis in water, and part B is concerned with the efficiency of ·OH production from these and other samples.

Part A. Microcrystalline TiO_2. The sample characteristics that result from the preparative procedure described above depend primarily on the temperature of hydrolysis and storage, as Table 1 indicates. In particular, the X-ray diffractograms in Figure 2 show that the crystalline material in samples I-R and II-R is rutile, whereas anatase is not present in detectable amounts.

Samples III-r and IV-a contain $\sim 15\%$ and $\sim 70\%$ anatase, respectively. Samples III-r and IV-a consist of aggregated spheroidal particles. By contrast, the transmission electron micrographs in Figures 3 and 4 show that the strongly aggregated primary particles in samples I-R and II-R are needle-shaped. This reflects the tendency of rutile to grow along its c axis (the [001] direction) and to form rods with square cross sections.[35] The longitudinal axis of the crystallites should therefore coincide with the c axis of the rutile lattice.

Appendix 1 shows that the barely formed crystallites in these aggregated rutile samples exhibit an increased bandgap due to
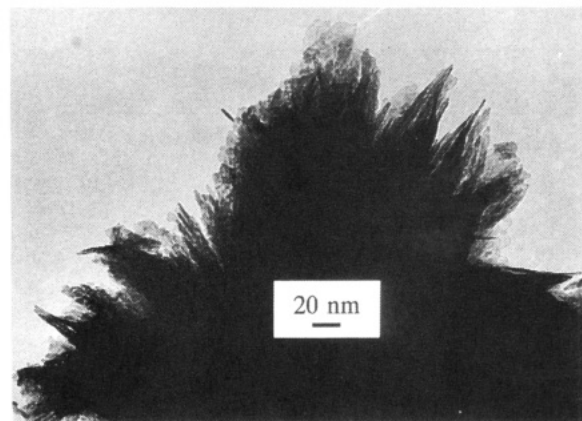

Figure 3. TEM image of the barely formed, tightly aggregated, and needle-shaped rutile crystallites in sample I-R. The contrast in this print emphasizes the needle tips that protrude from the aggregate.
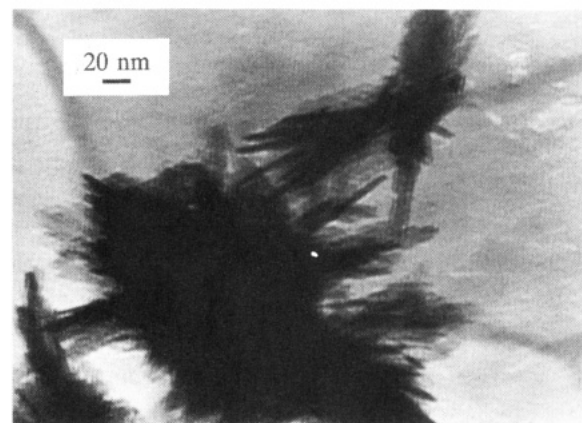

Figure 4. TEM image of the rutile needles in sample II-R.

size quantization in two dimensions. We should note that quantum-sized particles of *anatase* have been obtained before.[36,37] For rutile particles, bandgap increases of up to 0.093 eV have also been obtained.[38] However, the particle diameters of 5.5−10 nm reported in that study should preclude any quantum-size effects, suggesting that the effective crystallite size was significantly smaller than the particle size. Those particles, which were obtained from $TiCl_4$ hydrolysis in more acidic media, were not reported to be needle-shaped.

The important conclusion from appendix 1 is that more than 80% of the bandgap increase of ~ 0.14 eV should manifest itself as an increase in the oxidative power of holes at the valence-band edge. This should allow us to gauge the effect of that parameter on the photocatalytic efficiency of TiO_2 particles.

Specific Surface Areas. The aggregates of sample I-R (Figure 3) contain, apart from relatively well-formed needles, material that does not appear to be well crystallized and is characterized by a low contrast under the electron beam. This material is probably responsible for the low specific single-point BET surface areas of samples I-R through IV-a (*cf.* Table 1) and, in particular, for the fact that the measured surface area of sample I-R (143 m^2/g) is lower than that of sample II-R (220 m^2/g). For comparison, the calculated specific surface area of nonporous rutile rods with a diameter of 2 nm is ~ 500 m^2/g.

The outgassing of the samples at 350 °C prior to the single-point BET measurement also probably contributed to the low values. For example, Anpo *et al.*[38] report a marked effect of the calcination temperature on the effective diameter of small TiO_2 particles, even at temperatures below 350 °C. In a detailed analysis, Ooi *et al.*[39] showed that the BET surface areas of microcrystalline rutile and anatase, obtained after outgassing

Efficiency Variability in TiO2 Particles

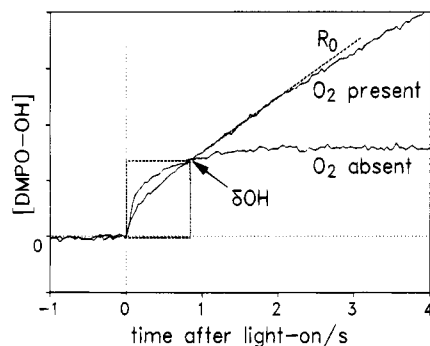*J. Phys. Chem., Vol. 99, No. 12, 1995* **4219**

Figure 5. Formation of DMPO-OH (arbitrary units) during the first seconds of irradiation, in the presence and in the absence of molecular oxygen at pH 7 and a TiO2 loading of 2 g/L. Method 2 of oxygen control was used, along with N2 or air bubbling for 18 h. For the purpose of these examples, an instrumental signal collect time of only 40 ms and a negligible time constant were used (*cf.* section 2).

at only 60 °C, do correspond to the actual surface areas of the primary particles. However, such low outgassing temperatures were not used in the present study, since the measurements were performed elsewhere, according to a standard BET procedure. Thus, the absolute specific surface areas of the samples, as used in the EPR experiments, are probably larger than those reported in Table 1. However, the relative values should be meaningful.

Part B. The First Seconds of •OH Photoproduction. Molecular Oxygen. The growth of the •OH spin-adduct concentration in irradiated suspensions of a particularly efficient TiO2 sample (P25-a) is shown in Figure 5. The two depicted cases correspond to the presence and to the absence of molecular oxygen, the only potential electron acceptor in solution.

For both cases, two phases of the DMPO-OH production are clearly distinguished. The first phase is a "pre-steady-state" production, and the second phase is the "steady-state" growth, characterized by an initial slope R_0. As is well established, R_0 vanishes if O2 and other potential electron acceptors are absent.[10,40] However, the much more efficient pre-steady-state •OH production *increases* further in efficiency if O2 is thoroughly purged from the system. This was found to be characteristic of the efficient anatase samples P25-a and A-A. Clearly, the reduced pre-steady-state efficiency in the presence of O2 indicates that •O2⁻ introduces a significant steady-state recombination route of the form of eq 6. Presumably, the most important "reactants" in that equation are adsorbed hydroxyl radicals.

The fact that O2 is not required for the pre-steady-state •OH production does not reflect slow O2 desorption from the particles or from the inner walls of the tubing: controlling the O2 concentration with methods 1 and 2 leads to equal DMPO-OH formation curves.

As a result of the less efficient pre-steady-state but more efficient steady-state •OH production in the presence of O2, the accumulated DMPO-OH concentration after almost 1 s of irradiation is independent of whether the suspension is air-saturated or depleted of O2. As indicated in Figure 5, this concentration is defined as the quantity δOH, which is of central interest to this study. It is measured with the standard procedure given in section 2.

Figure 6 depicts δOH for samples P25-a, A-A, I-R, and P9-R under various partial pressures of O2. One finds that δOH is practically independent of the O2 concentration within a wide range, which, as seen above for sample P25-a, includes the complete absence of O2. Thus, δOH is controlled by the competition of the oxidation and recombination reactions; electron-transfer reactions do not play a significant role.

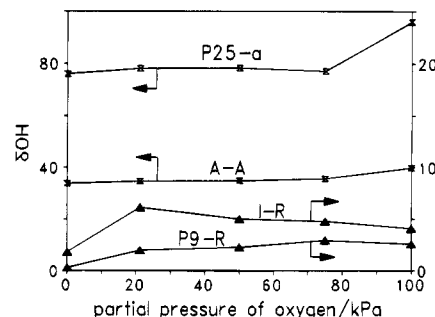**Figure 6.** δOH for samples P25-a, A-A, I-R, and P9-R as a function of O2 partial pressure. The lines are included as a guide for the eye; the arrows indicate the ordinate that applies to each sample (2 g/L, pH 7, errors ± 4).
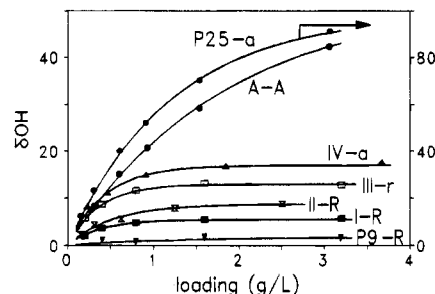

Figure 7. δOH for air-saturated suspensions at pH 7, as a function of TiO2 loading. The data points represent averages from independent measurements, resulting in estimated error margins of ±1. All curves (except for P25-a) refer to the left-hand ordinate. Sample R-R is not included since δOH could not be distinguished from noise in this case.

The dependence of δOH on the DMPO and phosphate concentrations, as well as the effect of pH and ultrasound, has also been studied. These results are available in the form of supplementary material. One finds that these parameters have marked effects. However, the differential effects on different samples are small when ultrasound and the phosphate buffer are used in preparing the suspensions.

Photon Absorption and TiO2 Loading. A comparison of the quantity δOH for air-equilibrated suspensions of the TiO2 samples described in Tables 1 and 2 is shown in Figure 7. The abscissa of this figure is the "TiO2 loading",[41] defined as the mass of TiO2 per unit of suspension volume.

The combined effect of light scattering and absorption within the suspension should follow an approximately exponential decay of the photon density along the net optical path. If, in addition, δOH $\propto I_a{}^\gamma$, where γ is a constant, then we may expect that the •OH production profile within the suspension is also given by an exponential decay. For sufficiently large irradiance, eq 12 predicted that $\gamma = {}^1/_2$ in the steady state, as is often found empirically.[17,42,43] If both conditions obtain even before the steady state, then it should be possible to fit the data points in Figure 7 to functions that show an exponential saturation with increasing TiO2 loading ϱ:

$$\delta\text{OH} = B\{1 - \exp(-\varrho/\varrho_0)\} \tag{13}$$

where B and ϱ_0 are the fitting parameters. The fitted curves are included in Figure 7, and one finds that they do indeed represent satisfactory fits. Hence, B is the expected value of δOH in the limiting case of very large loading, that is, when no light is transmitted through the suspension. ϱ_0 (g/L) is the loading at which δOH becomes $B(1 - e^{-1})$. The values of B and ϱ_0 for each sample are listed in Table 3, along with the values of the •OH production depth w. This production depth

TABLE 3: Fitting Parameters Used in Figure 7 and the "Production Depth" w^a

sample	B	ϱ_0, g/L	w, nm
P25-a	98 ± 5	1.24 ± 0.04	93 ± 6
A-A	52 ± 2.5	1.82 ± 0.07	130 ± 12
I-R	5.5 ± 0.25	0.40 ± 0.03	31 ± 6
II-R	8.5 ± 0.25	0.51 ± 0.03	39 ± 5
III-r	13 ± 0.25	0.37 ± 0.02	27 ± 4
IV-a	17 ± 0.25	0.43 ± 0.02	34 ± 4
P9-R	2.1 ± 0.5	1.2 ± 0.1	59 ± 34
R-R	~ 0		

^{a} The error margins were obtained by varying B and ϱ_0 within limits that provided reasonable fits to the data. The DMPO-OH formation for sample R-R could not be distinguished from noise.

may be obtained from ϱ_0 and γ, as described and discussed in appendix 2.

The fitting parameter B is of particular interest to this study. If the sample-to-sample variation in the absorbed photon flux I_a can be neglected in the limiting case of large loading, then B is proportional to the relative quantum efficiency of δOH for that case. The sample-to-sample variation in the spectral absorption was measured with the intergrating sphere method (*cf.* section 2). At photon energies above the sample bandgaps, this variation was estimated to be less than 5% of the mean value. Furthermore, for the lamp used in the EPR experiments, the spectral photon flux in the region of the interband transition onsets (i.e., 3.0 eV $< h\nu <$ 3.3 eV) is small compared to the flux at higher photon energies. We may therefore treat the sample-to-sample variations in I_a as a contribution to the experimental error. B then represents a direct estimate of the relative quantum efficiency of δOH at large loading.

Specific Surface Area. The value of B for a given sample is expected to be controlled in part by the specific surface area of that sample, and this is commonly observed.[65] However, the sample preparation is often more important and may mask any consistent effect of the specific surface area when samples of dissimilar origin are studied.[9] Furthermore, the photocatalytic efficiency of samples prepared under comparable conditions may reflect the specific surface area only up to a certain surface area value.[44]

The anatase-containing samples in the present study show no clear correlation between B and the BET surface areas (*cf.* Tables 1—3). For instance, one may compare the B values for samples A-A, P25-a, and IV-a. The respective surface areas arise essentially from the anatase particles since for P25-a and IV-a, which contain a small portion of rutile, the anatase particles are significantly smaller than those of rutile.[28] The surface area of both samples substantially exceed that of A-A. Nonetheless, P25-a is more and IV-a less efficient than A-A. Clearly, the preparative procedure has a stronger impact than does the specific surface area in this case.

The situation may be different for suspensions of rutile particles. The effective surface area of P9-R in suspension is likely intermediate between the BET value for this sample (2.24 m²/g) and that for untreated P25-a (54.0 m²/g), from which P9-R was obtained through heat treatment. This is suggested by the fact that intense ultrasound redisperses the particle agglomerates formed by sintering, as noticed by the improvement in suspension stability. Thus, δOH does appear to reflect the specific surface areas of the rutile samples R-R (no signal), P9-R, I-R, and II-R.

Quantum-Sized Rutile. Since δOH depends only on the rate constants for oxidation and recombination, it is particularly well suited for studying the effect of the oxidative power of valence band holes on the efficiency of ·OH formation.
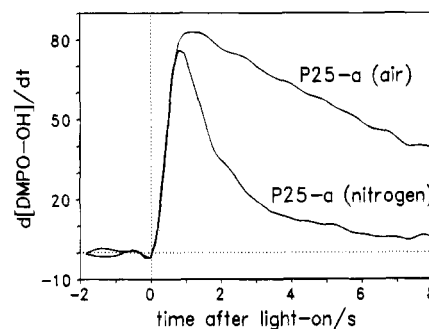

Figure 8. DMPO-OH formation rate (digital time derivative) for sample P25-a in the presence and in the absence of dissolved O_2.

Table 3 shows that the quantum-sized rutile samples I-R and II-R are significantly more efficient than are the non-quantum-sized samples P9-R and R-R. Using indices on B to identify the sample in question, we find $B_{\text{II-R}} \approx 4B_{\text{P9-R}}$ and $B_{\text{I-R}} > 2B_{\text{P9-R}} > B_{\text{R-R}}$, where $B_{\text{R-R}}$ was so low that it could not be distinguished from noise. Furthermore, $B_{\text{II-R}} \approx 0.5B_{\text{IV-a}}$, which is of interest since sample IV-a consists almost entirely of *anatase* particles.

This may appear to indicate that the hole oxidative power does play a significant role. However, as seen above, the values of B for the rutile samples also follow the trend of the specific surface areas, and this correlation clearly offers the most consistent explanation.[45] Thus, it is unlikely that the oxidative power of holes plays a major role in the efficiency of hydroxyl radical formation.[46] These results are consistent with those obtained by Anpo *et al.*,[38] who found that the efficiency increase for rutile samples with an increased bandgap largely followed the trend in specific surface area. In that report, the evidence for a bandgap effect was also not conclusive.

Steady State. The experiments in this study are best suited for the investigation of the pre-steady-state ·OH production, since the spin-adduct DMPO-OH is destroyed by UV light at rates that mask the steady-state production from the least-efficient samples. Nonetheless, some qualitative remarks may be made regarding the steady state, where the rates of oxidation and reduction must be equal.

In Figure 8, the DMPO-OH formation from sample P25-a is depicted in differentiated form, following the standard procedure for noise filtration. The two curves correspond to suspensions exposed to air or to N_2 bubbling for 18 h. One finds that the peak value, that is, δOH, is almost equal in both cases, as seen above. The shape of the curve for the O_2-deprived suspension is given entirely by the instrument settings and by the digital noise filtering. Thus, the steady-state rate must be judged from the DMPO-OH formation 5—8 s (i.e., several time constants) after light-on. This rate is significant if O_2 is present.

The corresponding curves for rutile samples always show the sharp rate decrease found for O_2-deprived P25-a, even when exposed to pure O_2 at ambient pressure. Samples with both crystal forms show intermediate values of δOH and R_0, as well as an intermediate ratio δOH/R_0. Thus, we find that, in a comparison of different TiO_2 samples, δOH and R_0 follow the same qualitative trend and that this trend is even more pronounced for R_0 than for δOH.

4. Discussion

Origin of δOH. In the absence of an electron acceptor in the aqueous phase, the DMPO-OH formation, which results in a final concentration of approximately δOH, implies a corresponding accumulation of free or trapped electrons on the particle. This corresponds to the photoinduced negative charge

Efficiency Variability in TiO$_2$ Particles

J. Phys. Chem., Vol. 99, No. 12, 1995 **4221**

of suspended TiO$_2$ particles as seen in electrophoretic experiments.[26,27,47]

Variations in B. The eight samples of TiO$_2$ particles investigated above show a wide range of •OH production efficiencies, both before and during the steady state. However, anatase samples are always more efficient than rutile samples.

The absolute quantum efficiency of steady-state •OH production from TiO$_2$ particles is usually far less than unity. For example, Sun[17] found that only ~4% of the photons absorbed by sample A-A in the steady state lead to the oxidation of methanol to formaldehyde via the methanol reaction with •OH under conditions similar to those of the present work. Thus, it is clear that recombination processes normally dominate the kinetics of photogenerated carriers, although exceptions have also been reported, for example by Lepore et al.[48]

These considerations do not imply that the different photocatalytic efficiencies correspond to different recombination rate constants. In particular, any model based on the assumptions that characterize the simplified model proposed by Gerischer[18] (eqs 2−7) will predict that variations in the rate constants for reduction or oxidation could be equally relevant. Regarding the validity of those assumptions we may note the following.

(1) Pseudo-First-Order Reduction. The rate of reduction cannot be greater than the rate of photon absorption. At our conditions of photon flux, only a few photons per second are absorbed by a 10-nm particle. The O$_2$ concentration at and near the particle surface should therefore always be in equilibrium with the aqueous phase. The latter concentration was controlled externally and should remain almost constant during the observation time.

(2) Pseudo-First-Order Oxidation. Here again, the very low rate of photon absorption by a small particle and the rapid reaction of •OH with DMPO strongly suggests that the density of adsorbed carrier acceptors (OH$^-$) will not vary during the first seconds of irradiation. Thus, the use of a pseudo-first-order rate constant is again appropriate. However, it should be stressed that the actual density of adsorbed OH$^-$ may vary from sample to sample. Hence, the pseudo-first-order oxidation rate constant (k_h) includes all of the sample specificity related to the oxidation process.

(3) Second-Order Recombination. Small TiO$_2$ particles in the dark should be depleted of "majority carriers", since the particle diameters are on the order of, or smaller than, the depletion layer width. Furthermore, the carrier densities that arise on absorption of a single photon can be extremely large, due to the small particle volume. This situation results in the condition of "high carrier injection", for which most recombination mechanisms predict second-order kinetics.[49] Evidently, if no carriers or carrier products accumulate, that is, if no carrier products remain adsorbed until the next photon is absorbed and if the number of electrons and holes per particle is always either zero or one, then recombination should be first-order. This may be the case for extremely small particles, prior to the steady state (cf. the approximately linear dependence of δOH on irradiance in the case of sample I). Nonetheless, the pronounced decrease in the efficiency of •OH production, observed during the establishment of a steady state, proves a corresponding increase in the efficiency of recombination. This implies that at least one type of carrier or carrier product does accumulate. Evidently, the degree of this accumulation depends on light intensity. Second-order recombination may thus be expected as an intrinsic property of very small TiO$_2$ particles.

In summary, the simple kinetic model used above should depict the essential kinetic features correctly, even if the actual reactions differ from those assumed by the model. We have
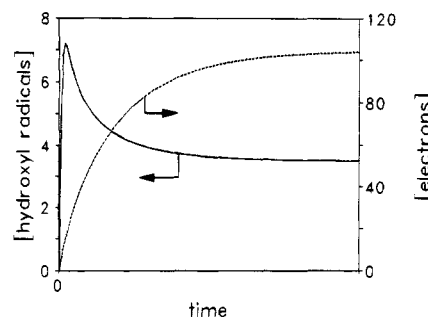
Figure 9. Expected evolution of the concentrations of hydroxyl radicals and conduction-band electrons when k_r and k_h are large but k_e is negligible.

seen that δOH repesents the relative number of •OH radicals produced in an irradiated suspension when electron acceptors are absent. This pre-steady-state •OH production depends on reactions 2−4 and 7 and therefore on the effective rate constants for oxidation and recombination; it does not depend on reactions 5 and 6, and the rate constant for reduction therefore does not play a role. Thus, the analysis of δOH (or B) and R$_0$ should allow us to decide if the natural variations in the steady-state photocatalytic efficiency of TiO$_2$ are primarily related to the rate constant for reduction or due to one or both of the other two rate constants.

Variations in B. Table 3 shows that B exhibits the pattern known for the steady-state efficiencies: anatase is more efficient than is rutile, and P25-a is particularly efficient. The variations in steady-state efficiency should therefore be due to variations in the rate constants which determine B, namely, those for oxidation and recombination but not that for reduction. In particular, the low steady-state efficiency of rutile is not primarily due to a larger "driving force" of electrons at the conduction-band edge of anatase.

Pre-Steady-State vs Steady-State •OH Production. If the simple kinetic model given in the Introduction does describe the essential elements of the system, we have according to eqs 2−7:

$$\frac{d[h^+]}{dt} + \frac{d[•OH]}{dt} = I_a - k_r[e^-][•OH] - k_h[•OH] \quad (14)$$

and

$$\frac{d[e^-]}{dt} = I_a - k_r[e^-][•OH] - k_e[e^-] \quad (15)$$

Figure 9 qualitatively depicts the time integrals of eqs 14 and 15 as a function of time, for the case of TiO$_2$, that is, for $k_h \gg k_e$ (cf. section 1). The accumulation of untrapped holes is neglected, since these carriers, which, under our conditions of particle size and irradiance, are created at rates smaller than 10^{-6} s^{-1} per particle, are trapped within hundreds of picoseconds.[50] Thus, the number of adsorbed hydroxyl radicals is expected to go through a pre-steady-state maximum and to then decrease due to recombination with electrons, whose concentration continues to increase until a large steady-state value is reached. This electron accumulation corresponds to the photoinduced negative charge observed in electrophoretic experiments;[26,27] it is also related to the fact that the effective lifetimes of untrapped electrons far exceed typical time constants for recombination in the bulk.[11,51]

Multiplication of the hydroxyl radical concentration by k_h should yield the overall oxidation rate (eq 4), and therefore the photocatalytic efficiency, as a function of time. We may vary
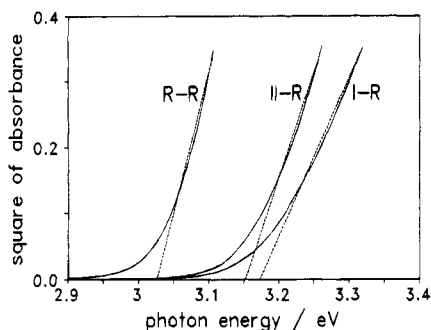
Figure 10. Interband absorption spectra of the quantum-sized rutile needles in samples I-R and II-R and of the non-quantum-sized rutile particles in sample R-R.

k_h, k_r, and k_e separately, so as to identify their respective effects on the pre-steady-state and steady-state productions of •OH. The results are as follows: (1) an increase in k_e has little or no effect on the maximum (pre-steady-state) oxidation rate and therefore on B; only R_0 increases; (2) an increase in k_h yields an increase in B and R_0 as well as an increase in the ratio B/R_0; (3) an increase in k_r also leads to an increase in the ratio B/R_0, but both quantities decrease.

Clearly, *variations in the rate constant for recombination* best represent the experimentally observed variations in efficiency within and between the anatase and rutile groups of samples: the smaller the pre-steady-state or steady-state efficiency of a sample, the larger the ratio between the two quantities.

Since the diffusion length of holes in TiO_2 single crystals far exceeds the particle dimensions in the present study,[52] it is very likely that the most relevant recombination processes are surface-bound. Thus, one may expect that, in particular, the greater quantum efficiency of anatase samples results from fewer or less efficient recombination centers at the anatase surface, compared to rutile. Our results do not distinguish between these possibilities. They do show, however, that the large natural variations in the overall photocatalytic efficiency of TiO_2 particles are related primarily to variations in the rate constants for recombination and not to those for carrier transfer.

5. Conclusions

The observation of a pre-steady-state photoproduction of hydroxyl radicals on TiO_2 particles emphasizes the usefulness of spin trapping with time-resolved electron paramagnetic resonance (EPR) for detection. The relative number of hydroxyl radicals produced in the absence of an electron acceptor was investigated in detail, and the steady-state efficiency in the presence of O_2 was studied more qualitatively. The analysis of these results strongly indicates that the efficiency variations that characterize TiO_2 samples of different origin or crystal form result primarily from variations in the effective rate constant for recombination (presumably at the surface), not of oxidation or reduction.

The effect of an increased oxidative power of holes on the efficiency of •OH production was studied by use of quantum-sized rutile particles. This increase (∼0.12 eV) appears to be the largest reported for rutile to date. However, the efficiency of •OH production does not increase beyond what may be expected as a result of the concurrent increase in specific surface area.

The pre-steady-state •OH production from the efficient samples studied (i.e., those that reduce O_2 at significant rates in the steady state) becomes most efficient when O_2 is purged from the suspension. This indicates that adsorbed •O_2^- radicals provide a significant route for recombination in those cases.

Appendix 1: Rutile "Quantum Wires"

Size Quantization for Rutile. For a spherical crystallite of radius R, Brus[53] obtained the following expression for the expected bandgap increase:

$$\Delta U_g \simeq \frac{h^2}{8R^2}\left(\frac{1}{m_e^*} + \frac{1}{m_h^*}\right) - \frac{1.8e^2}{4\pi\epsilon_0\epsilon_s R} \qquad (16)$$

where $m_e^* = 20\ m_e$ and $m_h^* = 3\ m_e$ are the effective electron[54] and hole[55] masses. The first two terms on the right-hand side are the carrier ground-state energies in a spherically symmetric quantum well of radius R. The third term represents the dielectrically screened attraction between the two carriers. For rutile spheres, $\epsilon_s \approx 0.33\epsilon_{||} + 0.66\epsilon_\perp = 117$, where $\epsilon_{||} = 89$ and $\epsilon_\perp = 173$ are measured along and perpendicular to the c axis.[56] Thus, an appreciable bandgap increase is expected for rutile only if the crystallite dimensions fall below ∼3 nm.[57] The primary particles in the aggregates of samples I-R and II-→R fulfill this condition in two dimensions and are therefore "quantum wires".

Needle-Shaped Crystallites. In analogy to eq 16, the bandgap increase for a needle-shaped crystallite of width a and of non-quantum-sized length should be[58]

$$\Delta U_g \simeq \frac{h^2}{4a^2}\left(\frac{1}{m_e^*} + \frac{1}{m_h^*}\right) \qquad (17)$$

where the dielectric term is neglected. This term is not significant in the crystallite-size range of interest, due to the large dielectric constants of rutile.

Equation 17 predicts what portions (ΔU_g^e and ΔU_g^H) of the bandgap increase (ΔU_g) are imparted to electrons and holes at the respective band edges. For electrons,

$$\Delta U_g^e \simeq \Delta U_g\left(\frac{m_h^*}{m_e^* + m_h^*}\right) \qquad (18)$$

Consequently, only ∼13% of ΔU_g will manifest itself as an increase in the electron reduction potential. The remainder will enhance the hole oxidative power.

Bandgap Increase. The interband absorption spectra of samples I-R and II-R and of sample R-R, which consists of large ("non-quantum-sized") particles, are given in Figure 10. The ordinate of this figure represents the square of the absorbance, which should be proportional to the excess photon energy ("direct bandgap").[59] The bandgap values were obtained by extrapolation (dashed lines).

With this method, we estimate bandgaps of 3.17 ± 0.02 eV for sample I-R and 3.15 ± 0.02 eV for sample II-R. The bandgap increase of ∼0.14 eV relative to bulk rutile exceeds the value of ∼0.09 eV, predicted by eq 17, for $a \approx 1.8$ nm.

Efficiency Variability in TiO₂ Particles

J. Phys. Chem., Vol. 99, No. 12, 1995 **4223**

This can be explained, at least partly, by the spread in particle widths (Table 1) and the fact that the bandgap varies as a^{-2}.

The empirical bandgap increase corresponds to two-thirds of the bandgap difference between rutile and anatase. According to eq 18, ΔU_g splits into $\Delta U_g^e \approx 0.02$ eV and $\Delta U_g^h \approx 0.12$ eV. Thus, ΔU_g^e is less than kT and therefore insignificant, whereas ΔU_g^h is large compared to kT. The hole oxidative power of these samples should approximate that of bulk anatase more closely than that of bulk rutile.

Appendix 2

It may be instructive to compare the near-UV penetration depth α^{-1} for a polycrystalline TiO₂ layer with the ·OH production depth w. If w is measured in terms of the depth of solid TiO₂ with density d along the net optical path within the EPR cell of length l, and if δOH $\propto I_a{}^\gamma$ and eq 13 apply, we expect

$$w = \frac{\varrho_0}{d}l = \frac{\alpha^{-1}}{\gamma} \tag{19}$$

The values of w are included in Table 3.

In principle, γ may be obtained by controlling the photon flux. Reducing the irradiance by ~50% reduces δOH of samples A-A and I-R to ~77% and ~55% of their values at full irradiance, respectively. This suggests that δOH from sample A-A follows the square-root dependence on irradiance, found to obtain for the steady-state rates of this sample,[17] as well as for P25-a.[42] In the case of sample I-R, the dependence of δOH on irradiance appears to be more linear. However, under our experimental conditions, the signal-to-noise ratio in δOH becomes too small for most samples if the irradiance is reduced further.

We may use eq 19, assuming that γ is in fact ~¹/₂ for samples A-A and P25-a and ~1 for samples I-R − IV-a. Then, practically all values of w fall within a rather narrow range. The value for sample A-A, which is the only exception, is an artifact: in that case, the particle diameter is ~150 nm so that the monolayer of particles needed to block the incident light will reflect the particle thickness, no matter how much smaller α^{-1} is.

Thus, the photon density profile, in terms of the TiO₂ depth, appears to be quite similar for all of the suspensions studied: γw is ~33 nm. Reported values of α^{-1} for polycrystalline TiO₂ films are 12-700 nm for photon energies of 4.81−3.25 eV.[60] A more detailed study of this topic would require intense monochromatic light and is outside the scope of this paper. However, we should note that w is a useful quantity. It provides the profile of the photocatalytic reaction and, if γ is known, the approximate profile of suprabandgap light within a given suspension. It is independent of the dimensions of the reaction flask and is merely a characteristic of the suspension in question.

References and Notes

(1) Jaegar, C. D.; Bard, A. J. *J. Phys. Chem.* **1979**, *83*, 3146.

(2) Izumi, I.; Fan, F.-R. F.; Bard, A. J. *J. Phys. Chem.* **1981**, *85*, 218.

(3) Legrini, O.; Oliveros, E.; Braun, A. M. *Chem. Rev.* **1993**, *93*, 671.

(4) Pelizzetti, E.; Minero, C. *Electrochim. Acta* **1993**, *38*, 47.

(5) Carey, J. H.; Lawrence, J.; Tosine, T. H. *Bull. Environ. Contam. Toxicol.* **1976**, *16*, 697.

(6) Fox, M. A.; Dulay, M. T. *Chem. Rev.* **1993**, *93*, 341.

(7) Bahnemann, D.; Cunningham, J.; Fox, M. A.; Pelizzetti, E.; Pichat, P.; Sepone, N. In *Aquatic and Surface Photochemistry*; Helz, G., Zepp, R., Crosby, D., Eds.; CRC: Boca Raton, FL, 1993; p 261.

(8) Sclafani, A.; Palmisano, L.; Schiavello, M. *J. Phys. Chem.* **1990**, *94*, 829.

(9) Tanaka, K.; Capule, M. F. V.; Hisanaga, T. *Chem. Phys. Lett.* **1991**, *187*, 73.

(10) Sclafani, A.; Palmisano, L.; Daví, E. *New J. Chem.* **1990**, *14*, 265.

(11) Schindler, K.-M.; Kunst, M. *J. Phys. Chem.* **1990**, *94*, 8222.

(12) Weil, J. A.; Bolton, J. R.; Wertz, J. E. *Electron Paramagnetic Resonance*; John Wiley & Sons: New York, 1994.

(13) Janzen, E. G. *Acc. Chem. Res.* **1971**, *4*, 31.

(14) Harbour, J. R.; Chow, V. S. F.; Bolton, J. R. *Can. J. Chem.* **1974**, *52*, 3549.

(15) Buxton, G. V.; Greenstock, C. L.; Helman, W. P.; Ross, A. B. *J. Phys. Chem. Ref. Data* **1988**, *17*, 717.

(16) Carmichael, A. J.; Makino, K.; Riesz, P. *Radiat. Res.* **1984**, *100*, 222.

(17) Sun, L. *Quantum Yield and Mechanism in TiO₂ Mediated Photocatalysis*. Ph.D. Thesis, The University of Western Ontario, London, Ontario, Canada, 1994.

(18) Gerischer, H. *Electrochim. Acta* **1993**, *38*, 3.

(19) Peterson, M. W.; Turner, J. A.; Nozik, A. J. *J. Phys. Chem.* **1991**, *95*, 221.

(20) Goldstein, S.; Czapski, G.; Rabani, J. *J. Phys. Chem.* **1994**, *98*, 6586.

(21) Warman, J. M.; de Haas, M. P.; Pichat, P.; Koster, T. P. M.; van der Zouwen-Assink, E. A.; Mackor, A.; Cooper, R. *Radiat. Phys. Chem.* **1991**, *37*, 433.

(22) Sun, L.; Schindler, K. M.; Hoy, A. R.; Bolton, J. R. In *Aquatic and Surface Photochemistry*; Helz, G., Zepp, R., Crosby, D., Eds.; CRC: Boca Raton, FL, 1993; p 409.

(23) Gerischer, H.; Heller, A. *J. Electrochem. Soc.* **1992**, *139*, 113.

(24) Gerischer, H.; Heller, A. *J. Phys. Chem.* **1991**, *95*, 5261.

(25) Kesselman, J. M.; Kumar, A.; Lewis, N. S. In *Photocatalytic Purification and Treatment of Water and Air*; Ollis, D. F., Al-Ekabi, H., Eds.; Elsevier: Amsterdam, 1993; p 19.

(26) Wang, C.-M.; Heller, A.; Gerischer, H. *J. Am. Chem. Soc.* **1992**, *114*, 5230.

(27) Dunn, W. W.; Aikawa, Y.; Bard, A. J. *J. Am. Chem. Soc.* **1981**, *103*, 3456.

(28) Datye, A. K.; Riegel, G.; Bolton, J. R.; Huang, M.; Prairie, M. R. *J. Solid State Chem.*, in press.

(29) Bickley, R. I.; Gonzalez-Carreno, T.; Lees, J. S.; Palmisano, L.; Tilley, R. J. D. *J. Solid State Chem.* **1991**, *92*, 178.

(30) Bird, M. I.; Longstaffe, F. J.; Fyfe, W. S. *Geochim. Cosmochim. Acta* **1993**, *57*, 3083.

(31) Fitzpatrick, R. W.; Le Roux, J.; Schwertmann, U. *Clays Clay Miner.* **1978**, *26*, 189.

(32) Spurr, A. R.; Myers, H. *Anal. Chem.* **1957**, *29*, 760.

(33) Klug, H. P.; Alexander, L. E. *X-Ray Diffraction Procedures*, 2nd ed.; Wiley & Sons: New York, 1974; p 687.

(34) Bolton, J. R.; Hoy, A. R. Personal communication.

(35) Moore, C. H. *Mining Eng.* **1949**, *1*, 194.

(36) Kormann, C.; Bahnemann, D. W.; Hoffmann, M. R. *J. Phys. Chem.* **1988**, *92*, 5196.

(37) Kavan, L.; Stoto, T.; Graetzel, M.; Fitzmaurice, D.; Shklover, V. *J. Phys. Chem.* **1993**, *37*, 9493.

(38) Anpo, M.; Shima, T.; Kodama, S.; Kubokawa, Y. *J. Phys. Chem.* **1987**, *91*, 4305.

(39) Ooi, K.; Katoh, S.; Sugasaka, K. *J. Colloid Interface Sci.* **1987**, *119*, 595.

(40) Brezowa, V.; Stasko, A.; Lapcik, L., Jr. *J. Photochem. Photobiol. A: Chem.* **1991**, *59*, 115.

(41) Sometimes the term "particle density" is used in the literature. We prefer the term "loading" so as not to be confused with the true density of solid TiO₂.

(42) Kormann, C.; Bahnemann, D. W.; Hoffmann, M. R. *Environ. Sci. Technol.* **1991**, *25*, 494.

(43) Egerton, T. A.; King, C. J. *J. Oil Colour Chem. Assoc.* **1979**, *62*, 386.

(44) Pichat, P.; Guillard, C.; Maillard, C.; Amalric, L.; D'Oliveira, J. C. In *Photocatalytic Purification and Treatment of Water and Air*; Ollis, D. F., Al-Ekabi, H., Eds.; Elsevier: Amsterdam, 1993; p 207.

(45) Note that $B_I < B_{II}$, although the hole oxidative power of sample I is equal or slightly larger than for sample II.

(46) For this reason, "delayed carrier thermalization",[57] which may result in additional oxidative and/or reductive power of carriers in quantum-sized crystallites, is not mentioned in the text.

(47) Jaffrezic-Renault, N.; Pichat, P.; Foissy, A.; Mercier, R. *J. Phys. Chem.* **1986**, *90*, 2733.

(48) Lepore, G. P.; Vlček, A., Jr.; Langford, C. H. In *Photocatalytic Purification and Treatment of Water and Air*; Ollis, D. F., Al-Ekabi, H., Eds.; Elsevier: Amsterdam, 1993; p 95.

(49) Bube, R. H. *Photoelectronic Properties of Semiconductors*; Cambridge University: Cambridge, 1992; Chapters 3−6.

(50) Rothenberger, G.; Moser, J.; Grätzel, M.; Serpone, N.; Sharma, D. K. *J. Am. Chem. Soc.* **1985**, *107*, 8054.

(51) Warman, J. M.; de Haas, M. P.; Pichat, P.; Serpone, N. *J. Phys. Chem.* **1991**, *95*, 8858.

(52) Marushka, H. P.; Ghosh, A. K. *Energy* **1978**, *20*, 443.

(53) Brus, L. *J. Phys. Chem.* **1986**, *90*, 2555.

(54) Itakura, M.; Niizeki, N.; Toyada, H.; Iwasaki, H. *Jpn. J. Appl. Phys.* **1967**, *6*, 311.

(55) Kasinski, J. J.; Gomez-Jahn, L. A.; Faran, K. J.; Gracewski, S. M.; Miller, R. J. D. *J. Chem. Phys.* **1989**, *90*, 1253.

(56) Boddy, P. J. *J. Electrochem. Soc.* **1968**, *115*, 199.

(57) Nozik, A. J. In *Photocatalytic Purification and Treatment of Water and Air*; Ollis, D. F., Al-Ekabi, H., Eds.; Elsevier: Amsterdam, 1993; p 39.

(58) See textbooks on quantum mechanics, such as: Dawydow, A. S. *Quantenmechanik*, 7th ed.; VEB Deutscher Verlag der Wissenschaften: Berlin, 1987; p 104.

(59) Sze, S. M. *Physics of Semiconductor Devices*, 2nd ed.; John Wiley & Sons: New York, 1981.

(60) Di Quarto, F.; Piazza, S.; Sunseri, C. *Electrochim. Acta* **1993**, *38*, 29.

(61) Abdullah, M.; Low, G. K.-C.; Matthews, R. W. *J. Phys. Chem.* **1990**, *94*, 6820.

(62) Munuera, G.; Moreno, F.; Gonzalez, F. In *Reactivity of Solids*; Anderson, J. S., Roberts, M. W., Stone, F. S., Eds.; Chapman and Hall: London, 1972; p 681.

(63) Yates, D. E.; Healey, T. W. *J. Chem. Soc., Faraday Trans. 1* **1980**, *76*, 9.

(64) Bérubé, Y. G.; DeBruyn, P. L. *J. Colloid Interface Sci.* **1968**, *27*, 305.

(65) Brown, G. T.; Darwent, J. R.; Fletcher, P. D. I. *J. Am. Chem. Soc.* **1985**, *107*, 6446.